Electronic Supplementary Material (ESI) for Nanoscale.

Supplementary Information for

Understanding the thermomechanical behavior of graphene-reinforced conjugated polymer nanocomposite via coarse-grained modeling

Yang Wang[a,b], Zhaofan Li[c], Dali Sun[d], Naisheng Jiang[a], Kangmin Niu[a], Andrea Giuntoli[b], and Wenjie Xia[c]

[a]School of Materials Science and Engineering, University of Science and Technology Beijing, Beijing, 100083, China

[b]Zernike Institute for Advanced Materials, University of Groningen, Groningen, 9747 AG, The Netherlands

[c]Department of Aerospace Engineering, Iowa State University, Ames, IA 50011, United States

[d]Department of Electrical and Computer Engineering, University of Denver, Denver, CO 80210, United States

[a,b,e]niukm@ustb.edu.cn, giuntoli@rug.nl, wxia@iastate.edu

Section S1. Bonded Interaction Optimization

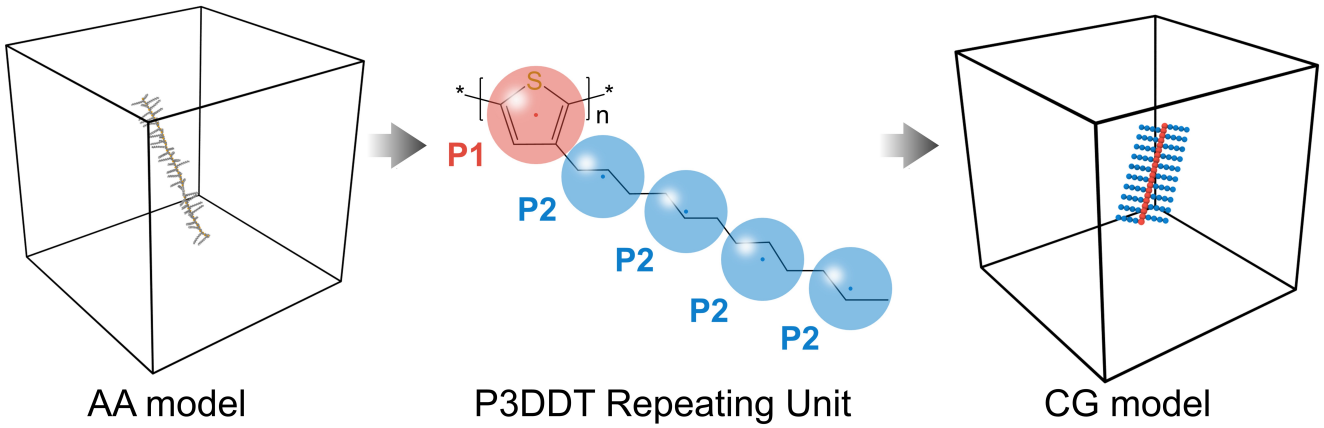

Fig. S1. The coarse-grained mapping procedure of P3DDT, following the same mapping scheme with the P3HT in the main manuscript.

For P3ATs with longer side chain lengths, *i.e.*, P3DDT, we performed AA and CG simulations to derive the extra CG bonded interactions based on the P3HT we developed before [1]. The mapping scheme of P3DDT is depicted in **Fig. S1**. For computation efficiency, we choose one P3DDT AA chain with 50 monomers in a cubic box. The Dreiding force field [2] containing bonded (bond, angle, and dihedral) and non-bonded terms are employed, and the Gasteiger method [3] is adopted to describe the atomic charges for electrostatic interactions:

$$U_{Total} = U_{bonded} + U_{nonbonded} = U_{bond} + U_{angle} + U_{dihedral} + U_{improper} + U_{nonbonded} \tag{1}$$

Specifically, all interactions in the Dreiding force field [2] have the following formula form:

$$U_{bond} = k_l(l - l_0)^2 \tag{2}$$

$$U_{angle} = k_\theta(\theta - \theta_0)^2 \tag{3}$$

$$U_{dihedral} = k_\phi[1 + d\cos(n\phi)] \tag{4}$$

$$U_{improper} = k_\chi(\chi - \chi_0)^2 \tag{5}$$

$$U_{nonbonded} = 4\epsilon\left[(\frac{\sigma}{r})^{12} - (\frac{\sigma}{r})^6\right] + \frac{Cq_iq_j}{\epsilon r} \tag{6}$$

It is noted that the AA force fields of OPLS-AA [4,5], COMPASS [6], DREIDING [7], GROMOS [8], et al. are used for the conjugated polymers, where the DREIDING force field is well parameterized and has been widely used to predict structures and dynamics of organic, biological, and inorganic molecules due to its general and simple function form. With the DREIDING force field, Orestis et al [7] studied the self-organization and structure of the

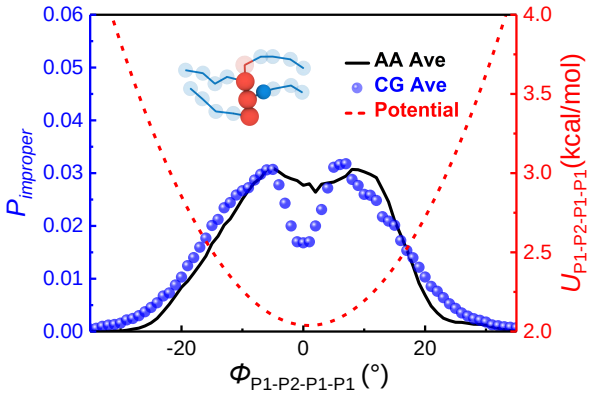

Fig. S2. Probability distributions of P1-P2-P1-P1 improper dihedral for the AA and CG P3AT model and corresponding potentials (red dotted line).

P3HT chain both in pure crystalline and pure amorphous phases, respectively. Additionally, Cao et al [9] utilized the DREIDING force field to explore the conformation behavior of conjugated polymer in implicit solvent. In this work, the cutoff distance is 12.0 Å for the AA simulation, and atoms in the same molecule separated by more than three bonds have the same nonbonded interactions (LJ + Coulombic) with each other as atoms on different molecules, atoms separated by one or two bonds have no nonbonded interactions with each other. Based on the defined CG mapping scheme, the target bonded probability distributions can be directly obtained through AA simulation. Then the CG bonded interactions are derived with IBM:

$$U_{i+1}(x) = U_i(x) + k_B T ln\left[\frac{P_i(x)}{P_{target}(x)}\right] \tag{7}$$

where k_B is the Boltzmann constant and T is the absolute temperature; the variable x refers to the bond length l, bond angle θ, dihedral angle ϕ, and improper dihedral χ respectively; $P_i(x)$ represents the relative probability distribution in ith iteration; $P_{target}(x)$ denotes the target probability distribution derived directly from AA simulation. Generally, several implementations of the IBM are needed to generate CG potential that can reproduce the probability distribution of AA models. **Fig. 2** in the main manuscript and **Fig. S2** show the probability distributions and corresponding CG potentials for the extra P2-P2-P2 angle term, P1-P1-P1-P2, P1-P2-P2-P2 and P2-P2-P2-P2 dihedral terms, and P1-P2-P1-P1 improper term. Specifically, the probability distribution functions of the P2-P2-P2 angle term are subject to multiple Gaussian distributions and thus implemented using a tabulated potential form. The dihedral terms of P1-P1-P1-P2, P1-P2-P2-P2, and P2-P2-P2-P2 are defined as

$$U_{dihedral}(\phi) = \sum_{i=1}^{5} a_i \cdot \cos^{i-1}(\phi) \tag{8}$$

where a_1 - a_5 stand for fitting constants. After 5-7 iterations using IBI, the bonded probability distributions of the CG model are fairly consistent with that of the AA counterpart. All corresponding parameters related

to the bonded interaction type are summarized in **Table S1**. The derived CG potential offers much improved computational efficiency compared to the AA model. It is noted that we choose N = 50 for P3DDT in order to get enough sampling data, and the repeating monomer of 20 for P3DDT will give us the same bonded interaction, as shown in **Fig. S3**. In our previous work [1], we used P3HT with 100 monomers per chain to derive the bonded interactions. And Zhang et al. [10] revealed that the CG potential of polystyrene-block-poly(methyl methacrylate) polymer with 40 repeating units per chain obtained at lower molecular weight can be safely transferred to the same polymer with higher molecular weight.

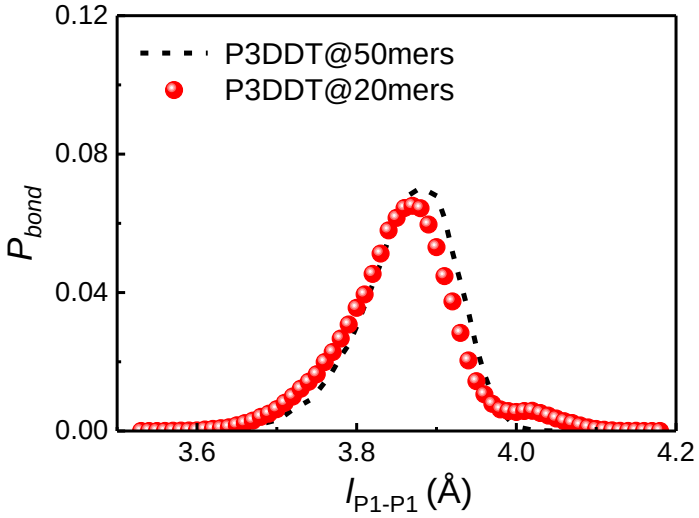

Fig. S3. Probability distributions of P1-P1 bond for the AA P3DDT model with 20 and 50 repeating units, respectively.

Section S2. Nonbonded Interaction Optimization

To get the initial estimations of nonbonded interactions, we built the liquid P3DDT monomer system. Namely, we put 800 P3DDT monomers in the system and derive the radial distribution functions of backbone bead P1 and sidechain bead P2, as shown in **Fig. S3**. The mainstream Lennard-Jones (LJ) potential is used to describe the nonbonded interactions between diverse CG beads:

$$E_{lj}(r,T) = 4\epsilon(T)\left\{\left[\frac{\sigma(T)}{r}\right]^{12} - \left[\frac{\sigma(T)}{r}\right]^{6}\right\} \tag{9}$$

where σ governs the effective van der Waals radius and marks the radial distance where the potential crosses the zero-energy line, and σ is the depth of the potential well (energy units) associated with the cohesive interaction strength of the materials. The energy switching function S_{LJ} is used in CG simulation to smoothly ramp the energy to zero between inner cutoff R_{inner} = 12 Å and outer cutoff R_{outer} = 15 Å. The CG model considers three different parameters for nonbonded interactions: σ_{11} and σ_{11} LJ parameters for backbone-backbone P1-P1

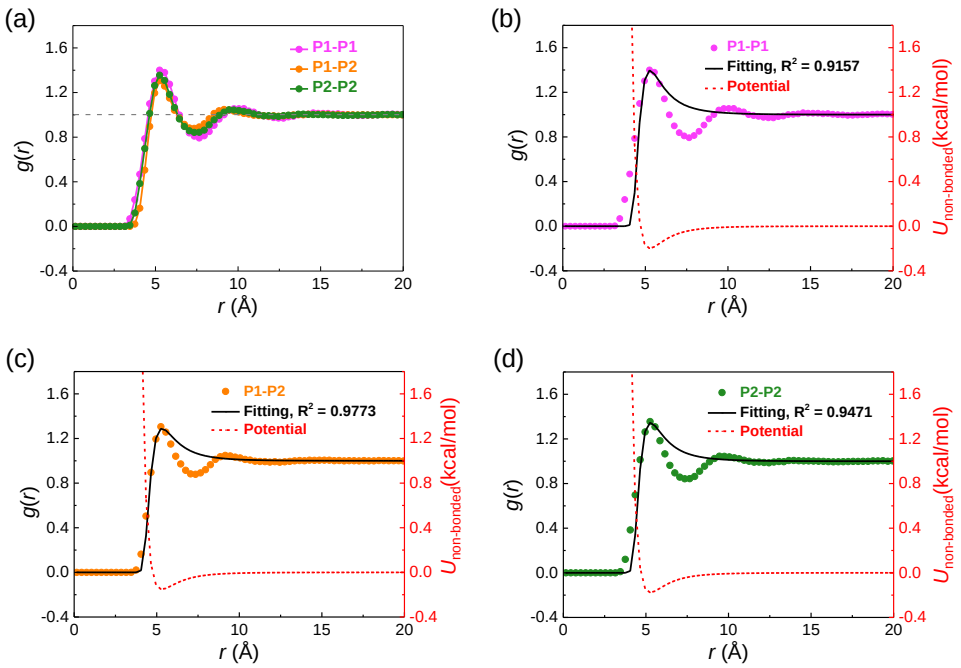

Fig. S4. (a) Radial distribution functions (RDF) $g(r)$ between effective bead centers P1-P1, P2-P2, and (b-d) their respective potentials obtained by fitting RDF with equation: $g(r) = exp\left\{-4\epsilon\left[(\frac{\sigma}{r})^{12} - (\frac{\sigma}{r})^{6}\right]/k_BT\right\}$, and then using Boltzmann inversion: $U_{nonbonded} = -k_BTln[g(r)]$. The initial non-bonded LJ parameters are determined: $\sigma_{11} = 4.69$ Å, $\sigma_{22} = 4.69$ Å, $\sigma_{12} = 4.73$ Å, $\epsilon_{11} = 0.199$ kcal/mol, $\epsilon_{22} = 0.177$ kcal/mol, and $\epsilon_{12} = 0.152$ kcal/mol. The subscript 1 and 2 denotes the P1 and P2 CG bead, respectively.

interactions; σ_{22} and σ_{22} for the sidechain-sidechain P2-P2 interactions; and the cross-interaction terms σ_{12} and $\sigma 12$ for the backbone-sidechain P1-P2 interactions. The cross-interaction terms are taken as the arithmetic average for $\sigma_{ij} = (\sigma_{ii} + \sigma_{jj})/2$ and the geometric average for $\epsilon_{ij} = \sqrt{(\epsilon_{ii}\epsilon_{jj})}$, respectively, where i and j denote different particle species. To achieve temperature transferability, we introduce the temperature rescaling factors $\beta(T)$ and $\alpha(T)$ for σ and ϵ, respectively. Therefore, the effective LJ parameters σ and ϵ are treated as a function of T by introducing "ER factors": $\sigma_{ii}(T) = \beta(T)\sigma^0_{ii}$, and $\epsilon_{ii}(T) = \alpha(T)\epsilon^0_{ii}$, where σ^0_{ii} and ϵ^0_{ii} are the initial estimates of nonbonded interaction generated by fitting an LJ potential to the inverted radial distribution function (RDF) of the AA system at 300 K using $U^0_{nonbonded}(r) = -k_BTln[g(r)]$ (**Fig. S3**).

As for the nonbonded interactions between graphene and P3AT, we utilized the cross-interaction terms taking the arithmetic average for $\sigma_{ij} = (\sigma_{ii} + \sigma_{jj})/2$ and the geometric average for $\epsilon_{ij} = \sqrt{\epsilon_{ii}\epsilon_{jj}}$, respectively. To quantify the interaction energy, we build the P3HT/graphene interlayer systems using AA and CG models, respectively, as shown in **Fig. S5**a. The interfacial energy is derived with $E_{interfacial} = \frac{-E_{P3HT-Gr}}{2*S_{graphene}}$, where $E_{P3HT-Gr}$ is the nonbonded interaction between graphene and P3HT, and $S_{graphene}$ is the area of graphene sheet. **Fig. S5**b shows the interaction energy between P3HT and graphene using AA and CG models, respectively, demonstrating the interfacial energy of the CG model is higher than the AA model. Additionally, we further characterize the interfacial energy contribution during the tensile mechanical test of P3HT/graphene nanocomposite with 5 wt% graphene content. **Fig. S5** shows the ratio of $E_{P3HT-Gr}$ compared with the total pair energy E_{pair} during the

stretching, revealing the small amount of $E_{P3HT-Gr}$ compared with E_{pair} and minor influence in our conclusion. However, it is important to highlight that the nonbonded interaction between P3HT and graphene should be reparametrized in the system where the interface plays a crucial role.

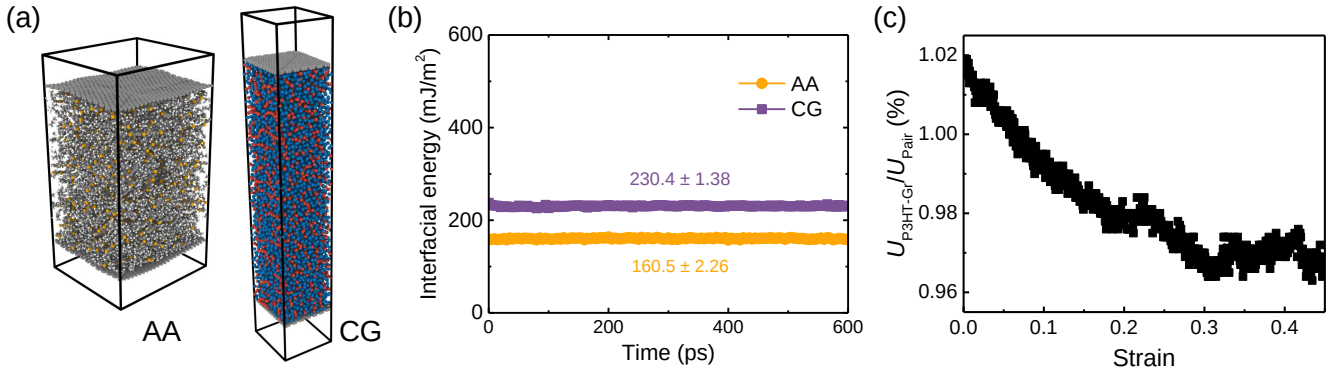

Fig. S5. (a) The snapshots of equilibrated AA and CG P3HT/graphene interface systems. (b) The interfacial energy evolution during the equilibration stage for AA and CG P3HT/graphene systems, respectively. (c) The interaction contribution of P3HT/graphene compared with total pair energy during the tensile deformation of P3HT/graphene nanocomposite with 5 wt% graphene content.

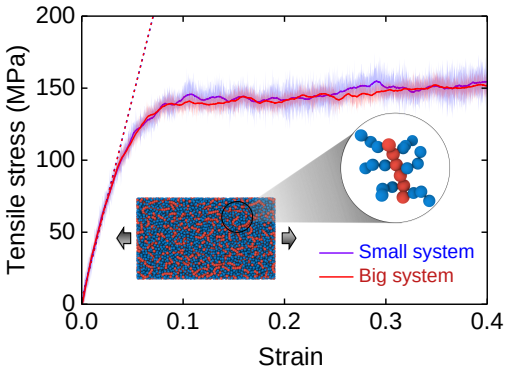

Fig. S6. Stress-strain curves (tensile deformation) of pristine 20-mer P3NT with different system sizes. The big and small systems stand for the systems containing 600 and 300 P3NT chains, respectively. Dashed lines represent the elastic stage's linear fitting, and the inset shows the final configuration of tensile deformation.

Section S3. P3HT/graphene nanocomposites

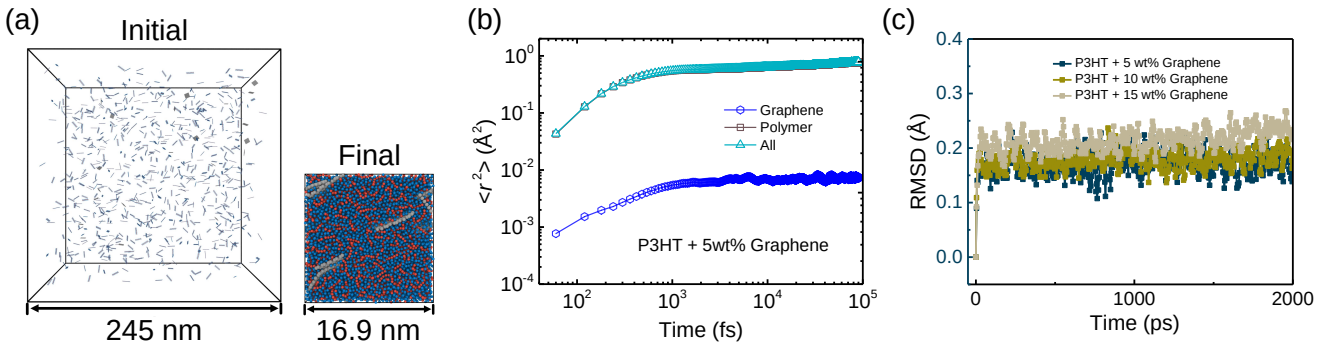

Fig. S7. (a) Initial and final configuration of the P3HT/graphene nanocomposite system with 5 wt% graphene content. (b) MSD curves of graphene and P3HT in P3HT/graphene nanocomposite with 5wt% graphene content. (c) Time series of the root-mean-square deviation (RMSD) of the center of mass of graphene for P3HT/graphene nanocomposites with different graphene loading in the final 2 ns production run (**Fig. 4**a in the main text).

Herein, we take P3HT/graphene nanocomposite with 5 wt% graphene content as a model system to illustrate the procedure for generating the simulation system. Firstly, we randomly packed 24 graphene sheets and 800 P3HT chains into a big simulation system with a box length of 245 nm to avoid the initial aggregation of the graphene sheet and the intersection of P3HT and graphene sheet (**Fig. S7**a). Then following the annealing, dynamics, and production run described in the main text, we can get the final nanocomposite system as the right panel shown in (**Fig. S7**a). To quantitatively measure how much graphene moves during the final 2 ns production run, we calculate the mean-square-displacement (MSD) of graphene, P3HT, and all CG beads, as shown in **Fig. S7**b. Additionally, we also calculated the root-mean-square deviation (RMSD) of the center of mass of graphene in P3HT/graphene systems with different graphene loading.

$$RMSD(t) = \sqrt{\frac{1}{N}\sum_{i=1}^{N} \mid C_i(t) - C_i(0) \mid^2} \tag{10}$$

where $C_i(t)$ and $C_i(0)$ denotes the center of mass of the i_{th} graphene sheet at time t and 0, N is the total number of graphene sheets in the system. The RMSD curves of graphene for P3HT/graphene systems with different graphene loading are shown in (**Fig. S7**c), demonstrating the stable and negligible movement of the graphene sheet due to the obstacle of the surrounding environment. Therefore, the final dispersion state is highly related to the initial configuration when the initial system is compact with high density.

Shen et al. [11]reported three scaling equations of the relationship between the density and Young's modulus of graphene foam, *i.e.*, (1) $E = \rho^{1.4}$, (2) $E = \rho^{2.55}$, (3) $E = \rho^{4.2}$. Additionally, a cubic scaling law is commonly observed in aerogels and aerogel composites, *i.e.*, (4) $E = \rho^3$. Next, we predict Young's modulus of P3HT/graphene nanocomposites using the above four relationships. As shown in **Fig. S8**, with the existing relationship of density and E, the Halpin-Tsai model shows overestimation and underestimation of E of P3HT/graphene nanocomposite

with different graphene content.

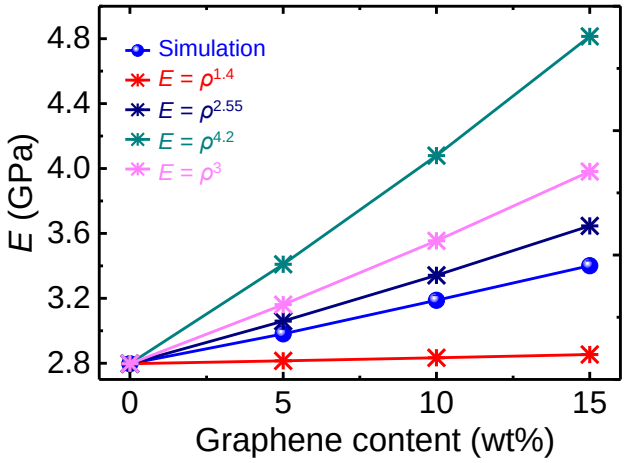

Fig. S8. Young's modulus of P3HT/graphene nanocomposite with different graphene contents. The predicted Young's modulus of P3HT/graphene nanocomposite using the Halpin-Tsai model with the intrinsic graphene density of 2.2 g/cm^3 and different equations of $E = \rho^n$

.

The mechanical deformation procedure utilized in the current work is the well-established protocol in many MD simulation works [12–19] although it is much higher than the experimental value due to current computational limitations. Therefore, the choice of strain rate of 0.5 ns^{-1} is a satisfactory compromise since the strain rate used in the experiment is unfortunately inaccessible to MD simulations, which is also in line with previous MD works [12–19]. Additionally, we conducted the tensile deformation test of pure P3HT using different strain rates and summarized the elastic moduli of P3HT from the experiment [20, 21] and simulation, [22–24]as shown in **Fig. S9**a,b. Results show that the simulation strain rate is much higher than the experiment, and a high strain rate would cause a stronger mechanical response. However, the elastic moduli of P3HT from simulation and experiment are still on the same order of magnitude, which is consistent with the discussion in previous work of combined experimental and analytical investigation of mechanical properties of amorphous polymers (polycarbonate and poly(methylmethacrylate)) [25].

Most importantly, in the current work, we mainly focus on the relationship between dynamical behavior and mechanical response of P3AT and corresponding graphene-reinforced nanocomposites, *i.e.*, stronger dynamics induce weaker mechanical properties. For comparison, we conducted the tensile test of pure P3HT using different strain rates of 5 and 0.05 ns^{-1}. As shown in **Fig. S9**c, a higher strain rate induces a higher Young's modulus of P3HT at each temperature we studied. However, different strain rate does not alter any conclusion of this work, *i.e.*, stronger dynamics induces weaker mechanical response. Additionally, we tested the orientation of the P3HT backbone and graphene of P3HT/graphene nanocomposite with 5wt% graphene content at 300 K using a strain rate of 5 ns^{-1}, showing the same conclusions as we obtained using 0.5 ns^{-1}.

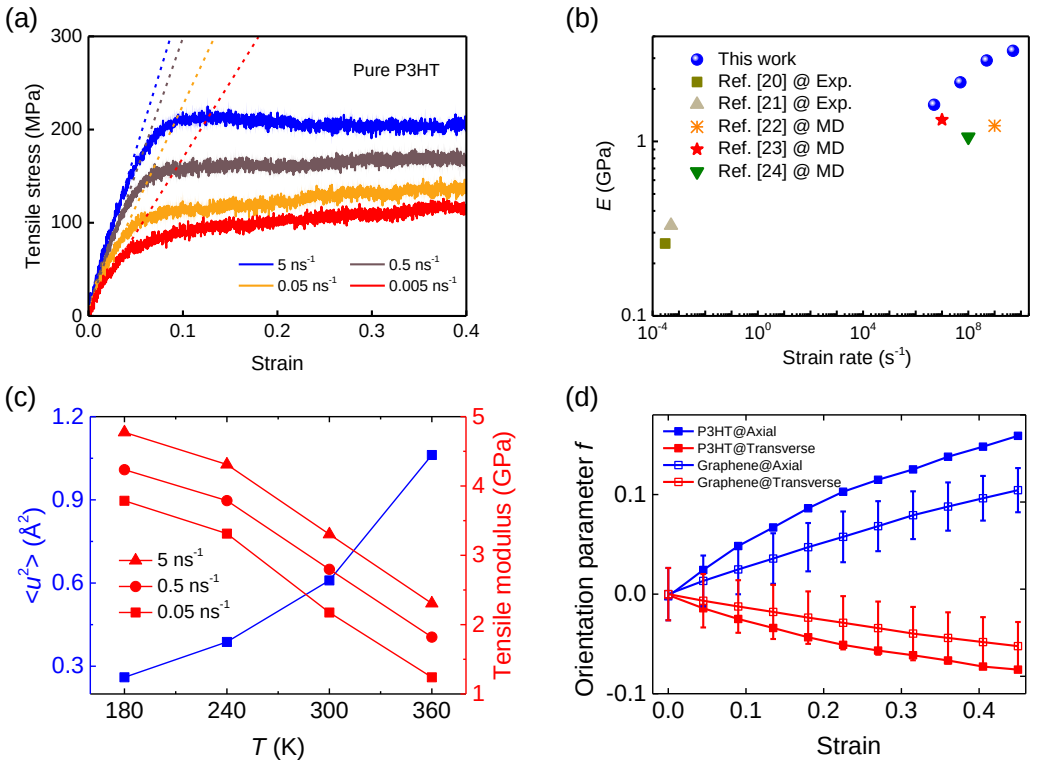

Fig. S9. (a) Stress-strain curves of pure P3HT system with different strain rates, with dashed lines showing the linear fitting of elastic region. (b) Comparison of Young's modulus of pure P3HT system from this work and published works. (c) The relationship between tensile modulus and Debye-Waller factor $\langle u^2 \rangle$ of pure P3HT under different strain rates. (d) Orientation behavior of P3HT backbone and graphene of P3HT/graphene nanocomposite system with 5wt% graphene content under the strain rate of 5 ns^{-1}.

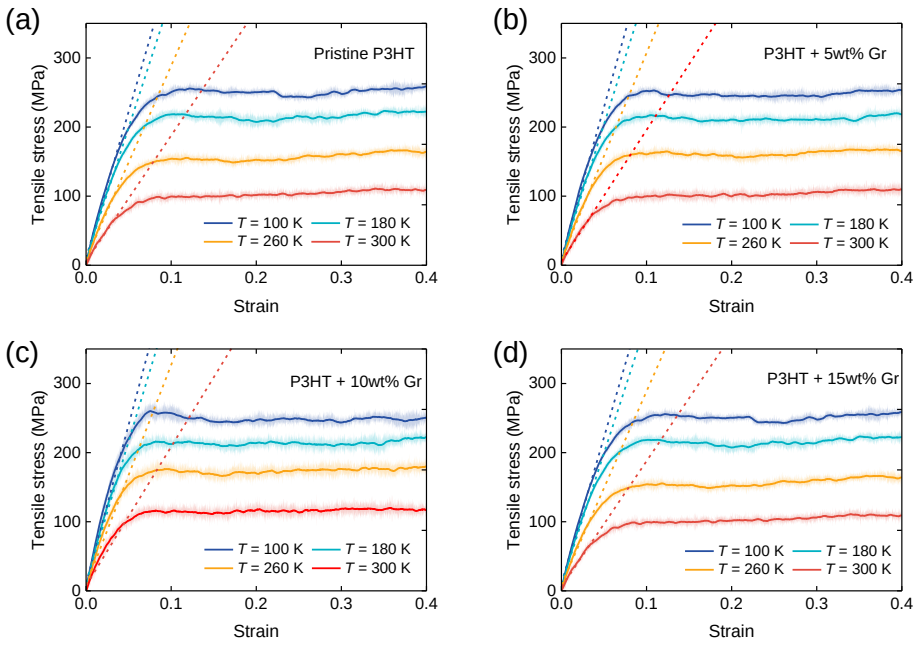

Fig. S10. Stress-strain curves (tensile deformation) of P3HT and P3HT/graphene nanocomposites under different temperatures and graphene contents. Dashed lines denote the elastic stage's linear fitting to obtain Young's modulus.

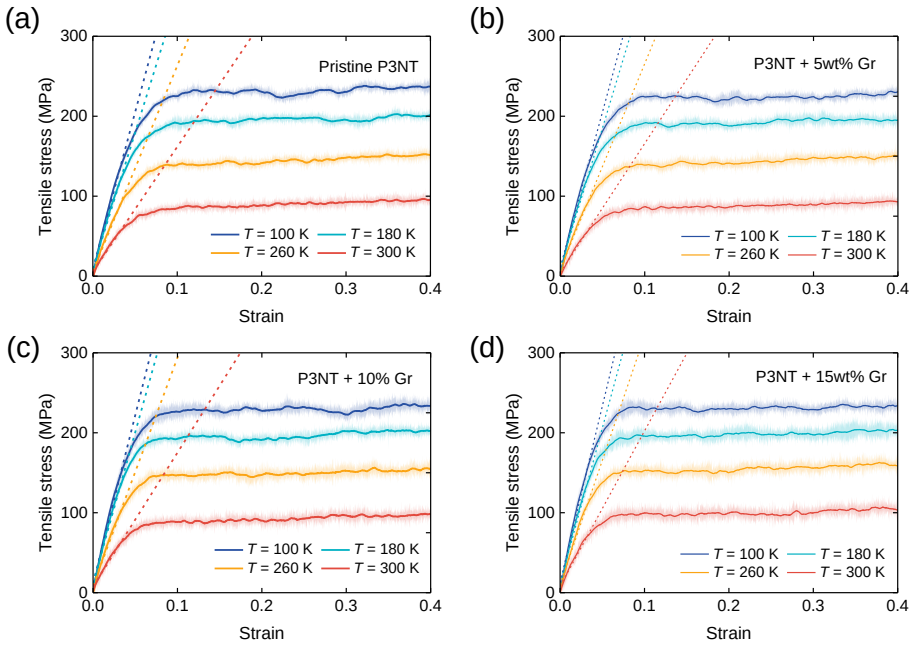

Fig. S11. Stress-strain curves (tensile deformation) of P3NT and P3NT/graphene nanocomposites under different temperatures and graphene contents. Dashed lines denote the linear fitting of the elastic stage to obtain Young's modulus.

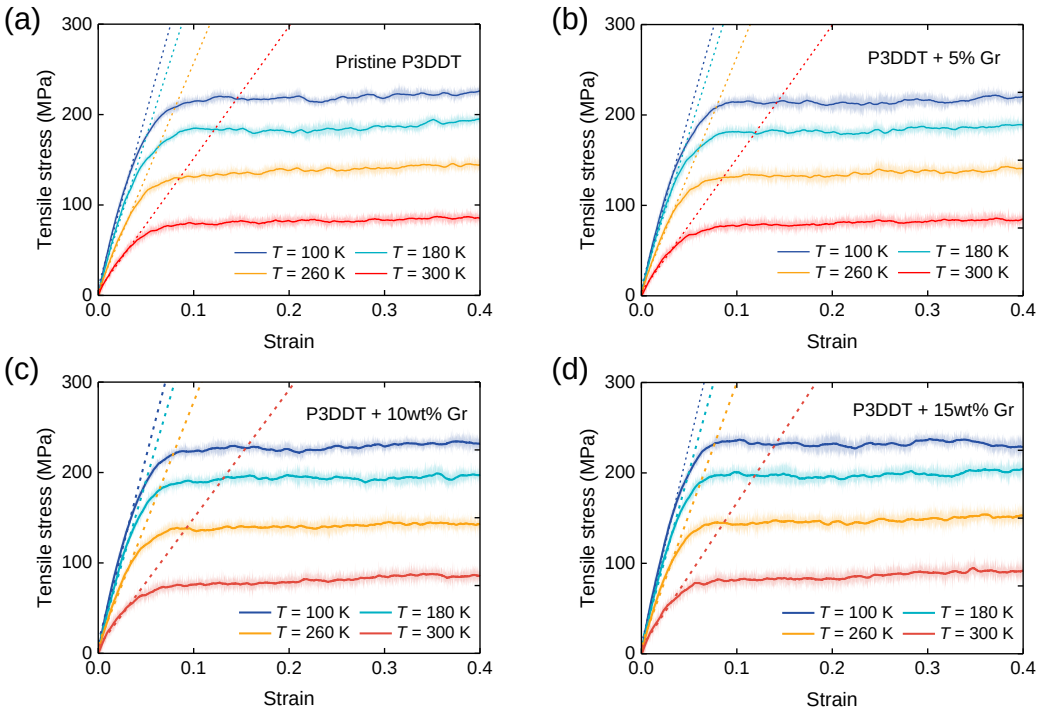

Fig. S12. Stress-strain curves (tensile deformation) of P3DDT and P3DDT/graphene nanocomposites under different temperatures and graphene contents. Dashed lines denote the linear fitting of the elastic stage to obtain Young's modulus.

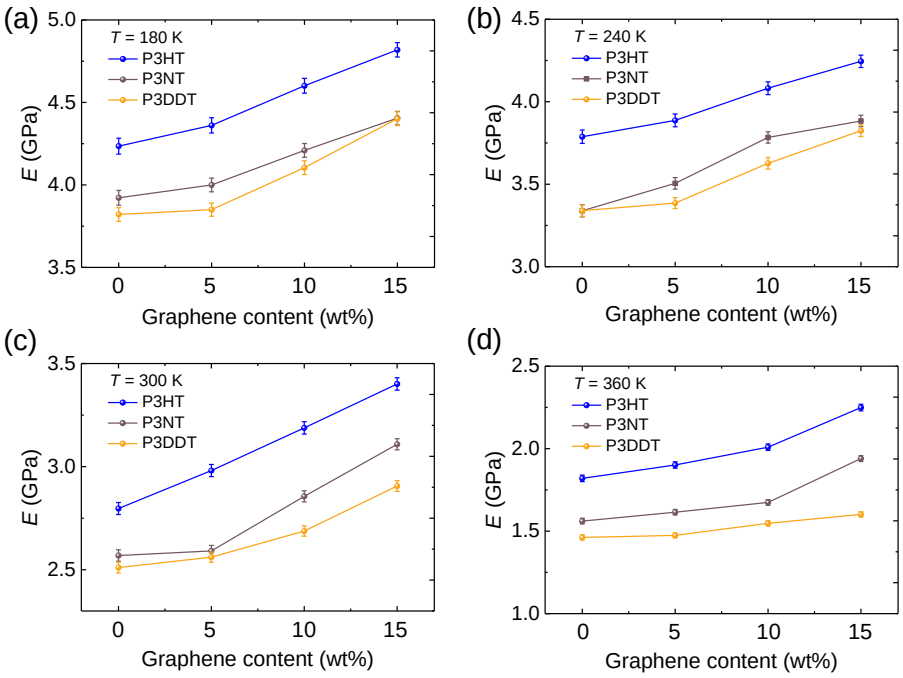

Fig. S13. Young's moduli variation of P3HT, P3NT, and P3DDT with different graphene contents of 0, 5, 10, and 15 wt% under (a) 180, (b) 240, (c) 300, and (d) 360 K, respectively.

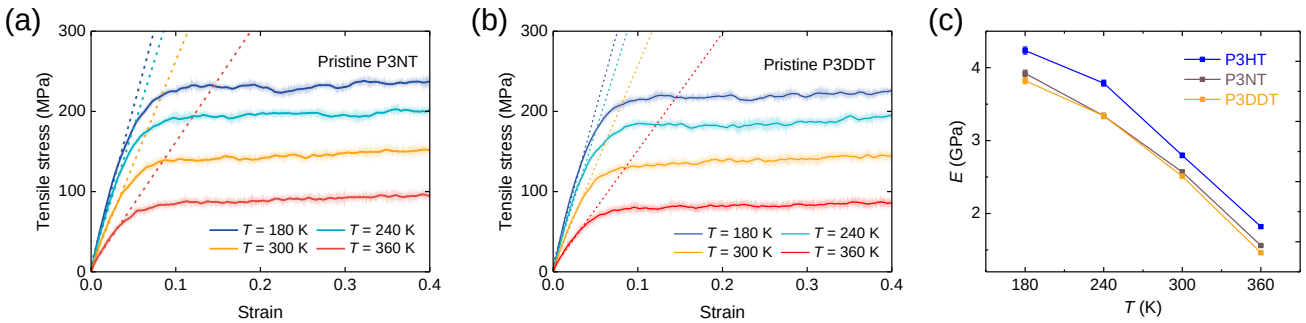

Fig. S14. Stress-strain curves (tensile deformation) of (a) pristine P3NT and (b) P3DDT systems under different temperatures. (c) Young's moduli variation of P3HT, P3NT, and P3DDT under different temperatures.

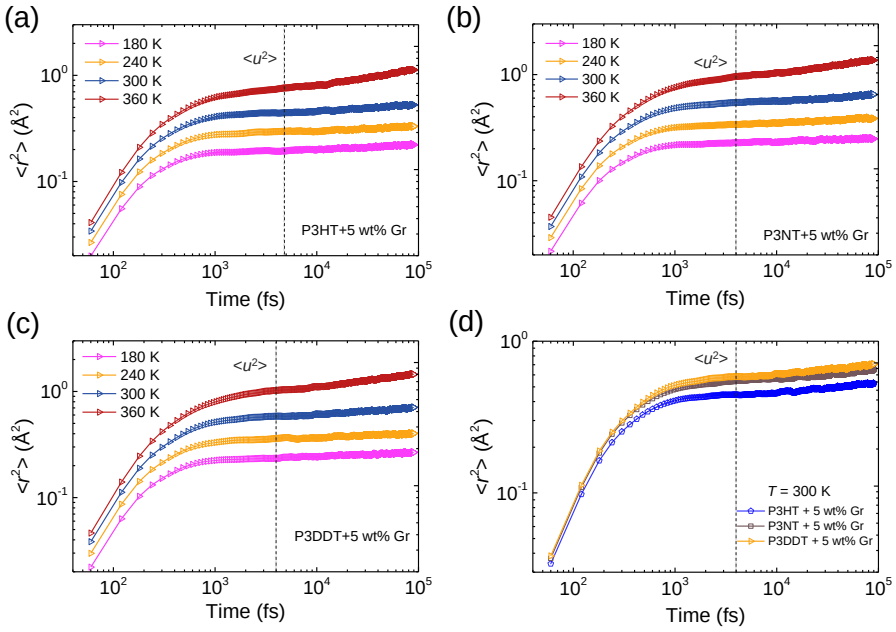

Fig. S15. Segmental MSD $\langle r^2 \rangle$ of the center of mass of CG bead vs t for the (a) P3HT/graphene, (b) P3NT/graphene, and (c) P3DDT/graphene nanocomposite systems with 5%wt graphene content under different temperatures. (d) Segmental MSD $\langle r^2 \rangle$ of the center of mass of CG bead vs. t for P3AT/graphene systems with different side chain lengths and 5%wt graphene content under 300 K. The vertical dashed line indicates $t = 4$ ps around the "caging" time, where $\langle u^2 \rangle$ is determined.

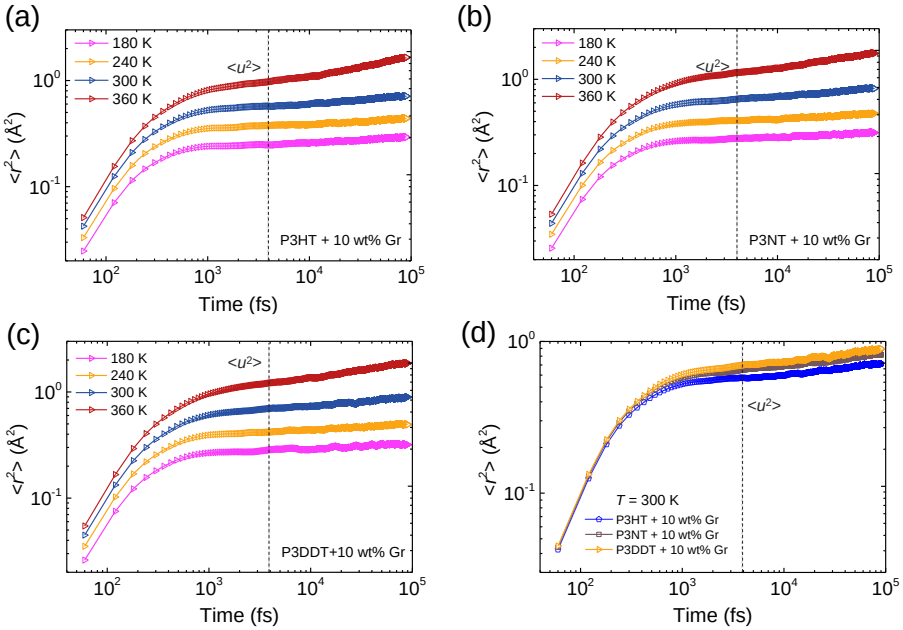

Fig. S16. Segmental MSD $\langle r^2 \rangle$ of the center of mass of CG bead vs t for the (a) P3HT/graphene, (b) P3NT/graphene, and (c) P3DDT/graphene nanocomposite systems with 10%wt graphene content under different temperatures. (d) Segmental MSD $\langle r^2 \rangle$ of the center of mass of CG bead vs. t for P3AT/graphene systems with different side chain lengths and 10%wt graphene content under 300 K. The vertical dashed line indicates $t = 4$ ps around the "caging" time, where $\langle u^2 \rangle$ is determined.

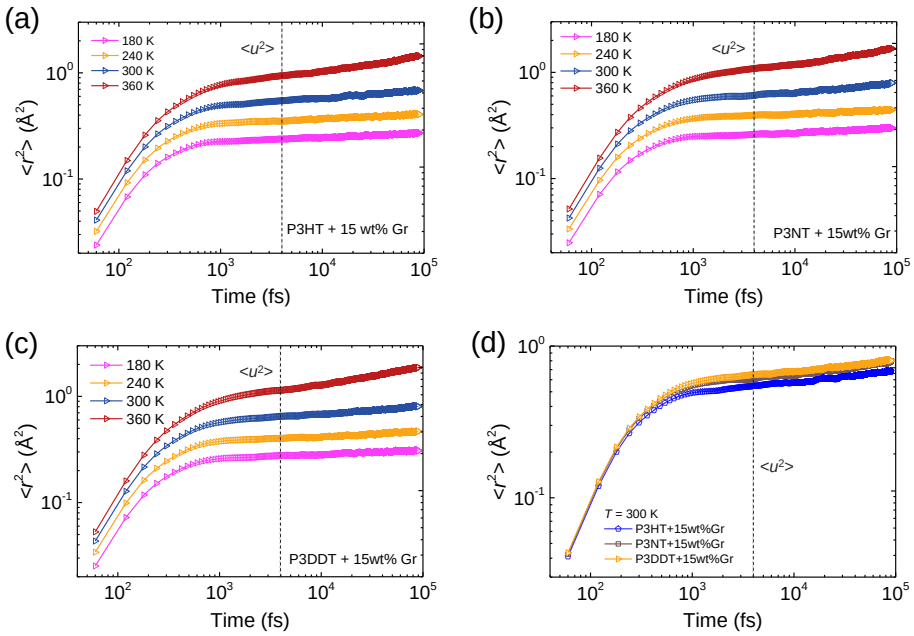

Fig. S17. Segmental MSD $\langle r^2 \rangle$ of the center of mass of CG bead vs t for the (a) P3HT/graphene, (b) P3NT/graphene, and (c) P3DDT/graphene nanocomposite systems with 15%wt graphene content under different temperatures. (d) Segmental MSD $\langle r^2 \rangle$ of the center of mass of CG bead vs. t for P3AT/graphene systems with different side chain lengths and 15%wt graphene content under 300 K. The vertical dashed line indicates $t =$ 4 ps around the "caging" time, where $\langle u^2 \rangle$ is determined.

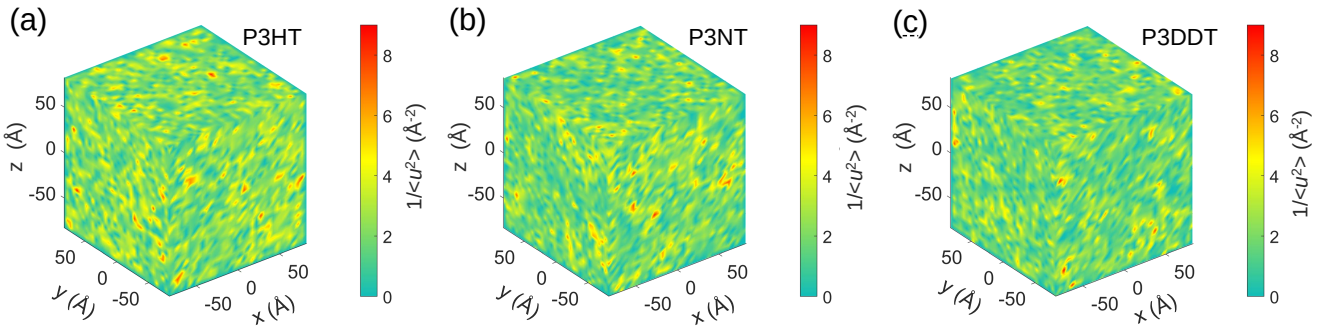

Fig. S18. Color maps of local stiffness $1/\langle u^2 \rangle$ of the center of mass of the CG beads of (a) pristine P3HT, (b) P3NT, and (c) P3DDT under 300 K. The color bar scale is the same for all plots.

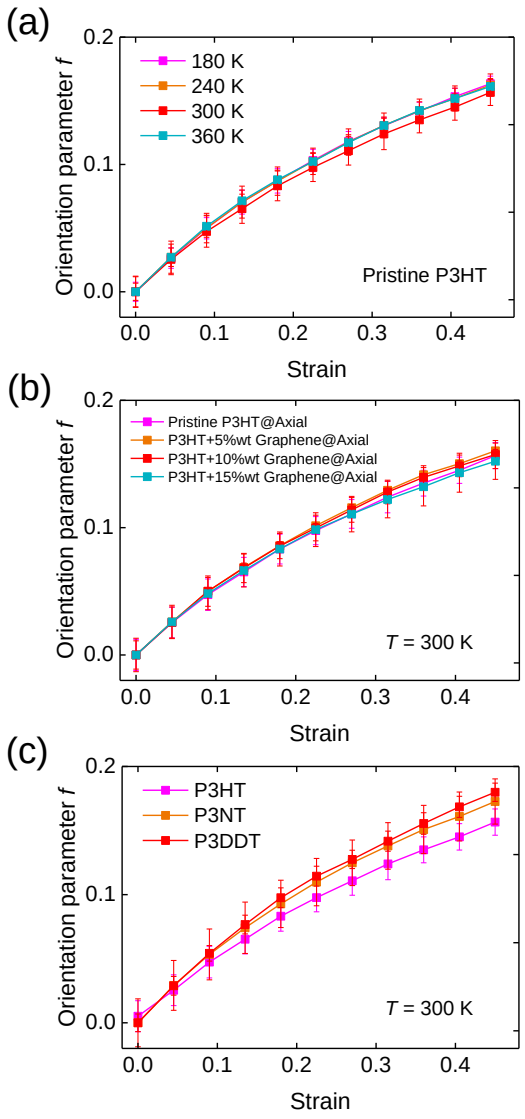

Fig. S19. Orientation parameter f of the axial component of (a) bulk pristine P3HT system under different temperatures, (b) P3HT/graphene nanocomposites with different graphene contents at 300 K, and (c) pristine P3ATs with different side chain length at 300 K.

Table S1. Functional Forms and Parameters of Bond, Angle, Dihedral, and Improper Interactions for CG Model of P3AT Conjugated Polymers.

Interaction	**Potential form**	**Parameters**
P1-P1 bond	$U_{\text{bond}}(l) = \sum_{i=2}^{4} k_i (l - l_0)^i$	$k_2 = 91.34$ kcal/mol $\cdot$ Å^2, $k_3 = 565.5$ kcal/mol $\cdot$ Å^3, $k_4 = 1825$ kcal/mol $\cdot$ Å^4, $l_0 = 3.871$ Å
P1-P2 bond		$k_2 = 67.08$ kcal/mol $\cdot$ Å^2, $k_3 = 240.9$ kcal/mol $\cdot$ Å^3, $k_4 = 225.3$ kcal/mol $\cdot$ Å^4, $l_0 = 4.092$ Å
P2-P2 bond		$k_2 = -39.74$ kcal/mol $\cdot$ Å^2, $k_3 = 31.83$ kcal/mol $\cdot$ Å^3, $k_4 = 964.6$ kcal/mol $\cdot$ Å^4, $l_0 = 3.822$ Å
P1-P1-P1 angle P1-P1-P2 angle P1-P2-P2 angle P2-P2-P2 angle	$U_{\text{angle}}(\theta) = -k_B T \ln \left\{ \sum_i^n \left[a_i \cdot \exp\left(\frac{-(\theta - \theta_0)^2}{b_i} \right) \right] \right\}$	$n = 3$, Tabulated form
P1-P1-P1-P1 dihedral	$U_{\text{dihedral}}(\phi) = \sum_{i=1}^{5} \left[a_i \cdot \cos^{i-1}(\phi) \right]$, unit: kcal/mol	$a_1 = 3.779$, $a_2 = -5.567 \times 10^{-1}$, $a_3 = -7.917 \times 10^{-1}$, $a_4 = 1.590 \times 10^{-1}$, $a_5 = 5.806 \times 10^{-1}$
P1-P1-P1-P2 dihedral		$a_1 = 3.160$, $a_2 = 3.426 \times 10^{-2}$, $a_3 = 8.339 \times 10^{-1}$, $a_4 = 7.080 \times 10^{-1}$, $a_5 = 7.807 \times 10^{-1}$
P1-P1-P2-P2 dihedral		$a_1 = 2.274$, $a_2 = -2.715 \times 10^{-1}$, $a_3 = 3.604$, $a_4 = -3.182 \times 10^{-1}$, $a_5 = 1.464$
P1-P2-P2-P2 dihedral		$a_1 = 3.613$, $a_2 = -4.873 \times 10^{-1}$, $a_3 = -5.413 \times 10^{-1}$, $a_4 = -3.445 \times 10^{-1}$, $a_5 = 5.222 \times 10^{-1}$
P2-P2-P2-P2 dihedral		$a_1 = 3.506$, $a_2 = -3.287 \times 10^{-1}$, $a_3 = -6.806 \times 10^{-2}$, $a_4 = 1.247 \times 10^{-1}$, $a_5 = 1.641 \times 10^{-1}$
P2-P1-P1-P2 dihedral		$a_1 = 4.658$, $a_2 = 9.223 \times 10^{-1}$, $a_3 = -1.762$, $a_4 = -7.527 \times 10^{-1}$, $a_4 = 1.639 \times 10^{-2}$
P1-P2-P1-P1 improper	$U_{\text{improper}}(\chi) = k_\chi \left[\chi - \chi_0 \right]^2$	$k_\chi = 2.142$ kcal/mol, $\chi_0 = 0^\circ$

Table S2. Parameters of TersoffCG(4-1) force field for 4-1 mapping CG graphene model [26].

Parameters	**TersoffCG(4-1)**
m	3
γ	1
λ_3 (Å^{-1})	0
c	38049
d	4.3484
$\cos\theta_0$	-0.57058
n	0.72751
β	0.00000015724
λ_2 (Å^{-1})	1.10595
B (kcal/mol)	31980.36
R (Å)	4.0
D (Å)	0
λ_1 (Å^{-1})	1.74395
A (kcal/mol)	128548.7

Table S3. The graphene dispersion state of [A, I, U] for P3HT/graphene nanocomposites with 5wt%, 10wt% and 15wt% graphene content, respectively. A, I, and U represent the percentage of graphene beads in each graphene sheet's dispersion state of Aggregated, Intercalated, and Unbound. The data in bold font indicates that the entire graphene sheet is in an Aggregated state, as shown in Fig. 4b in the main text.

5 wt% Graphene		10 wt% Graphene		15 wt% Graphene	
Graphene ID	[A,I,U]	Graphene ID	[A,I,U]	Graphene ID	[A,I,U]
1	[0.00, 0.07, 0.93]	1	[0.04, 0.26, 0.70]	1	[0.13, 0.35, 0.52]
2	[0.00, 0.09, 0.91]	2	[0.25, 0.51, 0.25]	2	[0.19, 0.42, 0.39]
3	[0.03, 0.48, 0.49]	3	[0.71, 0.26, 0.03]	3	[0.19, 0.41, 0.40]
4	[0.06, 0.19, 0.75]	4	[0.05, 0.34, 0.61]	4	[0.12, 0.65, 0.23]
5	[0.09, 0.21, 0.70]	5	[0.08, 0.25, 0.67]	5	[0.11, 0.29, 0.61]
6	[0.00, 0.04, 0.96]	6	[0.00, 0.06, 0.94]	6	[0.11, 0.71, 0.18]
7	[0.00, 0.00, 1.00]	7	[0.34, 0.56, 0.10]	7	[0.99, 0.01, 0.00]
8	[0.23, 0.29, 0.48]	8	[0.00, 0.00, 1.00]	8	[0.28, 0.52, 0.19]
9	[0.00, 0.01, 0.99]	9	[0.10, 0.21, 0.69]	9	[0.21, 0.78, 0.01]
10	[0.09, 0.41, 0.50]	10	[0.21, 0.62, 0.17]	10	[0.20, 0.27, 0.53]
11	[0.00, 0.07, 0.93]	11	[0.09, 0.28, 0.63]	11	[0.17, 0.35, 0.49]
12	[0.10, 0.20, 0.71]	12	[0.04, 0.40, 0.56]	12	**[1.00, 0.00, 0.00]**
		13	[0.00, 0.01, 0.99]	13	[0.00, 0.09, 0.91]
		14	[0.03, 0.15, 0.82]	14	[0.39, 0.31, 0.30]
		15	[0.00, 0.00, 1.00]	15	[0.65, 0.35, 0.00]
		16	[0.00, 0.07, 0.93]	16	[0.43, 0.55, 0.02]
		17	**[1.00, 0.00, 0.00]**	17	[0.39, 0.39, 0.22]
		18	[0.27, 0.50, 0.22]	18	[0.06, 0.23, 0.72]
		19	[0.00, 0.00, 1.00]	19	[0.00, 0.03, 0.97]
		20	[0.02, 0.24, 0.74]	20	[0.03, 0.31, 0.65]
		21	**[1.00, 0.00, 0.00]**	21	[0.41, 0.42, 0.17]
		22	[0.14, 0.37, 0.49]	22	[0.11, 0.74, 0.15]
		23	[0.76, 0.24, 0.00]	23	**[1.00, 0.00, 0.00]**
		24	[0.02, 0.46, 0.52]	24	**[1.00, 0.00, 0.00]**
				25	[0.00, 0.00, 1.00]
				26	[0.28, 0.36, 0.36]
				27	[0.40, 0.26, 0.34]
				28	[0.29, 0.69, 0.02]
				29	[0.17, 0.56, 0.27]
				30	[0.37, 0.40, 0.23]
				31	[0.18, 0.52, 0.30]
				32	**[1.00, 0.00, 0.00]**
				33	[0.06, 0.38, 0.56]
				34	[0.14, 0.25, 0.61]
				35	[0.33, 0.61, 0.06]
				36	[0.35, 0.48, 0.17]
				37	[0.33, 0.60, 0.07]
				38	[0.98, 0.02, 0.00]
				39	[0.04, 0.20, 0.76]

References

[1] Y. Wang, Z. Li, K. Niu, and W. Xia, Polymer **256**, 125159 (2022).

[2] S. L. Mayo, B. D. Olafson, and W. A. Goddard, J. Phys. Chem. **94**, 8897 (1990).

[3] J. Gasteiger and M. Marsili, Tetrahedron **36**, 3219 (1980).

[4] K. Do, D. M. Huang, R. Faller, and A. J. Moulé, Phys. Chem. Chem. Phys. **12**, 14735 (2010).

[5] D. M. Huang, R. Faller, K. Do, and A. J. Moulé, J. Chem. Theory Comput. **6**, 526 (2010).

[6] Q. Zhang, B. Mortazavi, X. Zhuang, and F. Aldakheel, Compos. Struct. **281**, 115004 (2022).

[7] O. Alexiadis and V. G. Mavrantzas, Macromolecules **46**, 2450 (2013).

[8] C. Oostenbrink, A. Villa, A. E. Mark, and W. F. Van Gunsteren, J. Comput. Chem. **25**, 1656 (2004).

[9] Z. Cao, S. A. Tolba, Z. Li, G. T. Mason, Y. Wang, C. Do, S. Rondeau-Gagné, W. Xia, and X. Gu, Adv. Mater. , 2302178 (2023).

[10] X.-Z. Zhang, Z.-Y. Lu, and H.-J. Qian, Macromolecules **56**, 3739 (2023).

[11] Z. Shen, H. Ye, C. Zhou, M. Kröger, and Y. Li, Nanotechnology **29**, 104001 (2018).

[12] W. Xia, F. Vargas-Lara, S. Keten, and J. F. Douglas, ACS nano **12**, 5427 (2018).

[13] D. D. Hsu, W. Xia, S. G. Arturo, and S. Keten, Macromolecules **48**, 3057 (2015).

[14] A. Giuntoli, N. K. Hansoge, A. van Beek, Z. Meng, W. Chen, and S. Keten, Npj Comput. Mater. **7**, 168 (2021).

[15] M. Dunbar and S. Keten, Macromolecules **53**, 9397 (2020).

[16] N. K. Hansoge, T. Huang, R. Sinko, W. Xia, W. Chen, and S. Keten, ACS nano **12**, 7946 (2018).

[17] W. Xia and T. Lan, Macromolecules **52**, 6547 (2019).

[18] Z. Li and W. Xia, Extreme Mech. Lett. **40**, 100942 (2020).

[19] Z. Li, Y. Wang, A. Alesadi, L. A. R. Pestana, and W. Xia, in *Fundamentals of Multiscale Modeling of Structural Materials*, Elsevier, 2023, pp. 75–111.

[20] D. Rodriquez, J. H. Kim, S. E. Root, Z. Fei, P. Boufflet, M. Heeney, T. S. Kim, and D. J. Lipomi, ACS Appl. Mater. Interfaces **9**, 8855 (2017).

[21] L. A. Galuska, E. S. Muckley, Z. Cao, D. F. Ehlenberg, Z. Qian, S. Zhang, S. Rondeau-Gagné, M. D. Phan, J. F. Ankner, I. N. Ivanov, et al., Nat. Commun. **12**, 2347 (2021).

[22] J. Munshi, T. Chien, W. Chen, and G. Balasubramanian, Soft Matter **16**, 6743 (2020).

[23] S. E. Root, S. Savagatrup, C. J. Pais, G. Arya, and D. J. Lipomi, Macromolecules **49**, 2886 (2016).

[24] Y. Yoshimoto, S. Sugiyama, S. Shimada, T. Kaneko, S. Takagi, and I. Kinefuchi, Macromolecules **54**, 958 (2021).

[25] A. D. Mulliken and M. C. Boyce, International journal of solids and structures **43**, 1331 (2006).

[26] Y. Wang, W. Nie, L. Wang, D. Zhang, K. Niu, and W. Xia, Comput. Mater. Sci. **222**, 112109 (2023).